Intermittency effects in a numerical simulation of stationary three-dimensional turbulence

By ERIC D. SIGGIA

Department of Physics, University of Pennsylvania, Philadelphia and
National Center for Atmospheric Research, Boulder, Colorado 80307†

AND G. S. PATTERSON

National Center for Atmospheric Research, Boulder, Colorado 80307

A Navier–Stokes direct spectral simulation code was modified to produce stationary and nearly isotropic turbulence in three dimensions. An approximate $-\frac{5}{3}$ energy spectrum was maintained over the entire range of wavenumbers by simultaneously driving the fluid and supplementing the ordinary viscosity with a subgrid-like energy sink in the last 15 % of the spectrum. Half-tone and contour plots of the fluctuations in the vorticity, rate-of-strain tensor and helicity show increasing 'spottiness' as the system evolves in time. Probability distributions and cross-correlations among these three quantities were also obtained. The flatness factor of the longitudinal velocity derivative, the longitudinal structure functions and the fluctuations in the locally averaged dissipation rate are consistent with some degree of intermittency, but do not unambiguously demonstrate its presence in the simulated flows.

1. Introduction

Large-scale numerical simulations have been used both to test the predictions of closure models (Orszag & Patterson 1972*a*, *b*; Herring & Kraichnan 1972) and to investigate numerous flows of engineering interest (see, for instance, the Proceedings of the 1977 Symposium on Turbulent Shear Flows held at Pennsylvania State University). The first extensive calculations for homogeneous isotropic turbulence were reported by Orszag & Patterson (1972*a*, *b*). They were restricted to a cubical mesh of 32^3 points and encompassed a range of 16 in wavenumber. In order to perform an 'honest' simulation, in which the molecular viscosity is used and for which truncation errors are negligible, R_λ was limited to around 40. In addition, only decay calculations were done.

Turbulent flows that are of practical interest are not homogeneous and isotropic and they are most often simulated with finite-difference codes, which are generally easier to implement than spectral methods. For shear-flow problems, one can let the mesh move with the mean velocity and use periodicity to fix the momentum and mass fluxes on opposite ends of the grid (Deardorff 1970; Schumann 1975). A subgrid parameterization is needed to account for the unresolvable scales of motion since R_λ is often quite large. Simulations of shear flows may be stationary, but they are not homogeneous and

---

† Present address: Laboratory of Atomic and Solid State Physics, Cornell University, Ithaca, New York 14853.

isotropic. If Orszag's (1971) argument, that N^3 Fourier modes are equivalent to a grid with $(2N)^3$ points, is accepted, then the code we use is competitive with the largest finite-difference codes currently running (Clark, Ferziger & Reynolds 1977).

The present study was in part motivated by a number of models that exhibited temporal intermittency when as few as four octaves in wavenumber were included (Siggia 1977, 1978). One would naturally like to see whether a numerical simulation would show any evidence of intermittency. A numerical experiment could yield both subjective manifestations of intermittency, such as spottiness in a half-tone or density plot, or more objective measures, such as the deviation of high-order structure functions from Kolmogorov's $-\frac{5}{3}$ law. Also, comparisons between different determinants of intermittency, which are not accessible with single hot-wire anemometer measurements, are possible. Irrespective of any connexion with intermittency, one can assess the correlations between the vorticity, rate-of-strain tensor, and helicity both visually and statistically.

Our simulation was performed with a direct spectral simulation code (Orszag & Patterson 1972 a, b) which had been trivially modified to produce stationary isotropic turbulence that was essentially homogeneous. To extract maximum information from the limited range of wavenumbers simulated, the largest modes present were driven, and we adjusted the dissipation to achieve stationarity. Stationary turbulence removes the uncertainties associated with a changing spectral shape and simplifies statistical averaging.

Two distinct techniques for forcing the system were implemented. Both were static (i.e. no stochastic forces were present) and produced a flow which was isotropic and homogeneous to a good approximation. The latter symmetries were imposed in order to achieve some resemblance to the small scales in a fully turbulent fluid in the small range of wavenumbers contained in the code.

Elimination of all truncation errors at large wavenumbers would require a viscosity so large that the entire energy spectrum would be considerably steeper than $-\frac{5}{3}$. Instead, a more realistic, though less controlled, simulation was done by adopting a subgrid-like parameterization to the direct spectral simulation code. We thus supplemented the viscosity with an additional damping that acts only on the upper 15 % of the spectrum. By adjusting parameters, it was possible to achieve a good approximation to a $-\frac{5}{3}$ law for all wavenumbers. For purposes of comparison we have also analysed data obtained from an 'honest' simulation in which the viscosity is the only source of damping and $R_\lambda \sim 40$. The numerical procedures and energy spectra are detailed in § 2.

As the system evolved, the velocity and vorticity vectors in real space were periodically archived. This permitted the later calculation of the strain tensor

$$e_{ij} = \tfrac{1}{2}(\partial_i v_j + \partial_j v_i)$$

and various other quantities. Samples of these data are displayed graphically in § 3. Histograms confirm that the vorticity and $\operatorname{tr} e^2$ $(= \sum_{i,j=1}^{3} e_{ij} e_{ji})$ in the evolved system are 'spottier' than they would be for a Gaussianly distributed random velocity field with the same energy spectra. Cross-correlation coefficients between ω^2, $\operatorname{tr} e^2$ and $|\mathbf{v}.\boldsymbol{\omega}|$ are also computed. A tabulation of flatness factors, longitudinal structure functions and dissipation fluctuations concludes § 3.

2. Numerical methods and energy spectra

Details of the direct spectral simulation have been discussed in a number of papers (Orszag & Patterson 1972*a, b*; Riley & Patterson 1974; Schumann & Patterson 1978*a, b*; Pouquet & Patterson 1978), and we shall reiterate only a few salient features that are particularly relevant to our calculation. The fluid is confined to a box of side π cm and periodically continued. Physical units are employed for ease of comprehension. The units of length and time can be rescaled to match the kinematic viscosity to any particular fluid. The velocity is represented either in terms of 32^3 Fourier modes or on a lattice of 32^3 points. The wavenumber range is effectively from 2 to $2 \times 242^{\frac{1}{2}} \simeq 31\cdot1$. The upper limit is slightly less than 32 to simplify the removal of aliased interactions (Patterson & Orszag 1971).

The available wave vectors are conventionally divided into 15 shells

$$2n \leqslant k < 2n+2, \quad n = 1, 2, \dots 14,$$

with
$$30 \leqslant k \leqslant 2 \times 242^{\frac{1}{2}}. \tag{2.1}$$

Energy spectra were drawn from a plot of the 15 points representing shell averages of $\frac{1}{2}v_k v_{-k}$, where $\mathbf{v}_k$ is the velocity in Fourier space. There is a noticeable amount of statistical scatter in the energies of the first two shells since they represent averages over only 26 and 66 Fourier modes, respectively. The last shell is incomplete and contains 1662 modes instead of 3074. The energy in the last shell was multiplied by the appropriate ratio in drawing spectra.

To compute the initial velocity, half the available wavenumbers were selected such that no two were related under reflexion in the origin. Six Gaussianly distributed random numbers were chosen for the real and imaginary parts of $\mathbf{v}_k$. The longitudinal part of $\mathbf{v}_k$ was projected out and the transverse part scaled to produce a $-\frac{5}{3}$ spectrum. The relation $\mathbf{v}_{-k} = \mathbf{v}_k^*$ was used to fix $\mathbf{v}_{-k}$.

The time differencing was done by a leapfrog method with a time step of $0\cdot01$ s for $\langle v^2 \rangle \sim 3$. The optimal time step was found empirically. Smaller steps increased the accuracy only slightly, while somewhat larger steps resulted in a numerical instability. A single time step required about 6 s on a CDC 7600 computer.

We wish to drive the largest wavenumbers in our system in as homogeneous and isotropic a manner as possible. Anisotropies and inhomogeneities in the large scales are expected to relax as the cascade proceeds, but a range of only 16 in wavenumber is insufficient for this to occur. The stochastic driving forces used in statistical theories are awkward to implement numerically and not generally realized experimentally. A large-scale shear is more common experimentally but inhomogeneous, while wind-tunnel experiments are non-stationary. The compromise we adopted, which is trivial to implement numerically, was to freeze the first shell of wavenumbers at their initial values. A static and reasonably isotropic shear results that drives the remaining modes. A randomly sheared flow is not strictly homogeneous in the absence of an average over the large scales. However, in our one realization, the kinetic energy appeared to be uniformly distributed in space and small-scale properties were indistinguishable from results obtained by a second method of forcing [see (2.3)] that does result in homogeneity.

Our technique for continuously stirring the system can be regarded either as an isotropic version of the usual shear flow or as a model of the eddies several cascade

	Large scales	Small scales
Run 1	0·328–0·341	0·330–0·339
	0·323–0·343	0·322–0·342
	0·298–0·364	0·328–0·338
	0·313–0·351	0·328–0·337
Run 2	0·269–0·441	0·320–0·352
	0·269–0·393	0·326–0·345
	0·308–0·372	0·331–0·337
	0·300–0·360	0·331–0·336

TABLE 1. Degree of large- and small-scale isotropy for runs 1 and 2. Corresponding data are given in table 2 and figures 3 and 5. Shown in the first and second columns are the minimum and maximum of $\langle v_i^2 \rangle / \sum_{i=1}^{3} \langle v_i^2 \rangle$ and $\langle \omega_i^2 \rangle / \sum_{i=1}^{3} \langle \omega_i^2 \rangle$ respectively for $T = 0, 4\cdot0, 6\cdot0$ and $8\cdot0$ s. The velocity and vorticity are representative of the large and small scales respectively. The first shell of wavenumbers was frozen at its initial value, which proved to be quite isotropic in the first run but evolved according to (2.3) in the second run. This explains the greater variability of $\langle v_i^2 \rangle / \sum_{i=1}^{3} \langle v_i^2 \rangle$ in the second run. There was no obvious correlation between the directions of the maximum or minimum components at different times. The isotropic relationship $\langle \omega^2 \rangle / \langle \mathrm{tr}\, e^2 \rangle = 2$ was satisfied to within a fraction of a per cent at all times.
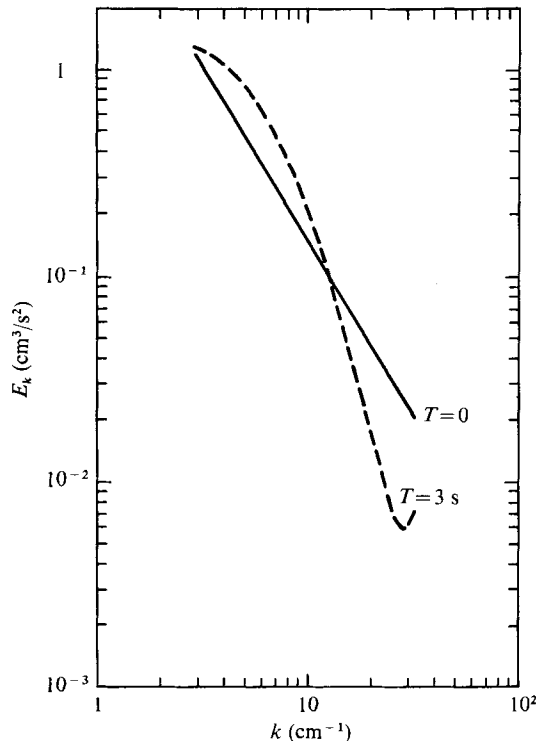

FIGURE 1. Sample energy spectrum of turbulence driven by the same static random shear as in run 1 (cf. figure 3) but with $\nu = 0\cdot008\,\mathrm{cm^2/s}$ and no additional damping. The system has equilibrated by $T = 3\cdot0$ s and is characterized by $R_\lambda = 42$, skewness $= 0\cdot43$ and Kolmogorov microscale $= 39\,\mathrm{cm^{-1}}$. A $-\frac{5}{3}$ spectrum (solid line) is drawn for comparison.
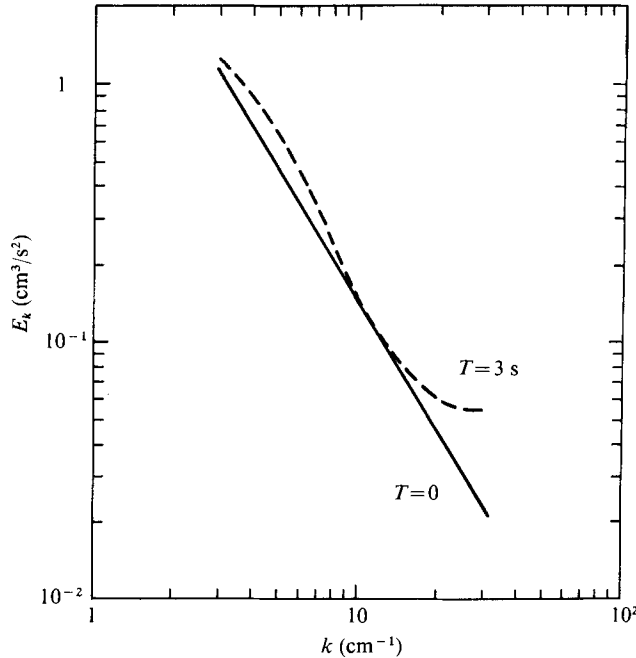
FIGURE 2. Energy spectrum of turbulence subject to the same random shear and viscosity ($\nu = 0.0034$) as run 1 (cf. figure 3) but with no additional damping. The flow is statistically stationary by $T = 3.0$ s. The excess energy at large k is a characteristic truncation effect when the viscosity is too small. The initial spectrum is almost coincident with the solid line, whose slope is $-\frac{5}{3}$.

steps down from the largest anisotropic ones. The latter viewpoint is somewhat inadequate since the first shell is frozen in a randomly chosen configuration which in reality would evolve, though more slowly than the other modes in the system. The largest modes are Gaussianly distributed and necessarily do not contribute to such quantities as the skewness. This last shortcoming might have been remedied by letting all the modes evolve for a short time and then freezing the first shell.

In the course of the numerical integration, several measures of isotropy were monitored (table 1). Angle brackets will henceforth denote a spatial average at a fixed time. The lack of isotropy in the initial data represents inherent sampling errors and suggests what degree of anisotropy is significant. The three independent second-order longitudinal structure functions and the six transverse ones (i.e. x and y velocities separated along the z axis, etc.) agreed to within 5 % at all separations.

It has frequently been noted that using too small a viscosity in a simulation causes the energy spectrum to increase at the largest wavenumbers, which is indicative of a tendency towards statistical equipartition. A viscosity large enough to eliminate truncation errors would result in a spectrum representative more of the dissipation range than of the inertial range. Figures 1 and 2 illustrate these possibilities.

To obtain position-space data that would best correspond to real turbulence, an additional source of damping was added in the last few shells to eliminate the 'tail' in figure 2. It proved surprisingly easy to match a $-\frac{5}{3}$ law by adjusting ν and α in the following expression:

$$d\mathbf{v}_k/dt = \ldots - \nu k^2 \mathbf{v}_k - \alpha(k^2 - k_d^2)^2 \eta(k - k_d) \mathbf{v}_k, \qquad (2.2)$$

	Run 1	Run 2 (a)	Run 2 (b)
Integration times (s)	0–9·0	0–5·5	7·0–11·0
Dissipation parameters, equation (2.2)			
ν (cm²/s)	0·0034	0·0025	
α (cm⁴/s)	$1·275 \times 10^{-4}$	$9·375 \times 10^{-5}$	
k_d (cm⁻¹)	26·0	25·38	
Characteristic times (s)			
$\pi/v_{r.m.s.}$	1·7	2·2	2·6
$(\pi^2/\epsilon_i)^{\frac{1}{3}}$	2·1	2·6	3·0
$1/\omega_{r.m.s.}$	0·058	0·055	0·09
$1/(\mathrm{tr}\,e^2)^{\frac{1}{2}}$	0·083	0·10	0·12
Characteristic lengths (cm) (wavenumbers, cm⁻¹)			
Size of box	3·14	3·14	3·14
Integral scale	0·57	0·64	0·61
Taylor microscale	0·25	0·25	0·26
$(\epsilon_i/\nu^3)^{\frac{1}{4}}$	73	77	70
Other parameters			
Skewness	0·36	0·33	0·34
R_λ	75	90	80
ϵ_i (cm²/s³)	1·17	0·56	0·35
ϵ_d/ϵ_i	0·76–1·02	0·80–0·96	0·80–0·95

TABLE 2. Some characteristic parameters for the run driven by a random shear, run 1, and the case with linear forcing (equation (2.3) with $\Omega = 0·4\,\mathrm{s}^{-1}$), run 2. The energy spectrum for the first run is given in figure 3. The two separate entries for run 2 correspond to the upper and lower curves in figure 5. Consult the text for details. The rate of energy input is denoted by ϵ_i and the rate of energy dissipation by the viscosity ν by ϵ_d. Except for α and k_d, all other parameters are defined conventionally (see Orszag & Patterson 1972b; or Batchelor 1953, chap. 3). When appropriate, parameters refer to times for which the system appears to be statistically stationary. Statistical fluctuations are generally of order 5 % in most quantities.

where the dots represent the nonlinear terms. The step function η is one when its argument is positive and zero otherwise. The values of ν, α and k_d which we used are given in table 2. The supplemental damping rises smoothly from zero and is appreciable only in the outermost two shells. There is a tendency for the energy in the thirteenth shell to be a bit larger than it should be for this reason. A damping which increased as $k^2 - k_d^2$ would probably have worked equally well. If ν was too small, but α sufficiently large to make the last few shells scale properly with respect to the large scales, the energy spectrum appeared flat for intermediate wavenumbers.

A quantitative measure of the relative importance of the two terms in (2.2) is given by the ratio of ϵ_i and ϵ_d (the energy input and dissipation rates); see table 2. Approximately 85 % of the energy fed into the system by the static shear is dissipated by the ordinary viscosity.

We believe that for $T \gtrsim 2·5\,\mathrm{s}$ the randomly sheared model is statistically stationary and furthermore that the energy spectrum is intrinsic and independent of initial conditions. Figure 3 shows the energy spectrum and the scale of fluctuations. A number of characteristic times are given in table 2. Those applicable to the large scales are something of an overestimate since the largest modes that are free to evolve
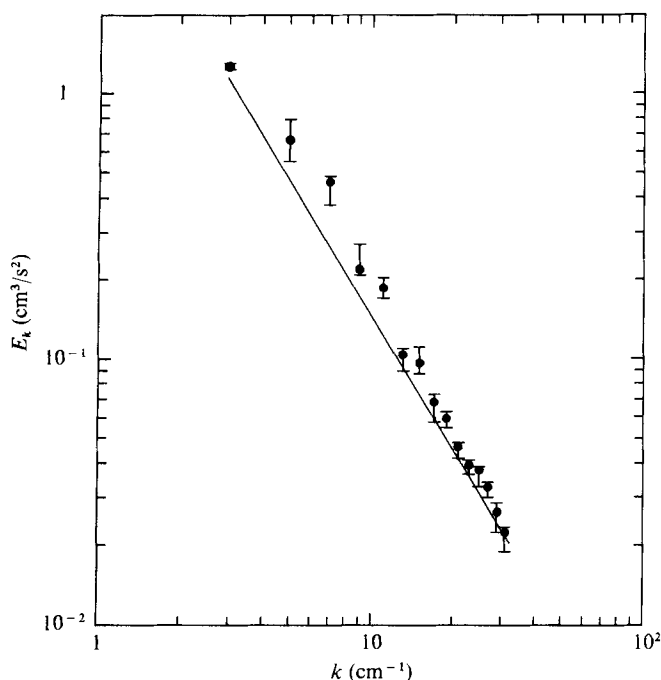
FIGURE 3. Energy spectrum of the turbulence driven by a random shear for run 1 (cf. table 2). The solid line shows what a $-\frac{5}{3}$ spectrum would look like when plotted from values for averages over the 15 shells defined in (2.1). The initial spectrum nearly coincides with the solid line. The points show the spectrum at $T = 4 \cdot 0$ s. The error bars are set at the maximum and minimum of the shell-averaged energies for $3 \cdot 0 \leqslant T \leqslant 9 \cdot 0$ s.

have a minimum wave vector of 4 rather than 2. Another measure of the equilibration time is provided by figure 4, which shows the evolution of a random shear-driven flow with an initial spectrum cut-off at $k \sim 10$. Different initial conditions resulted in somewhat less static shear than was present in figure 3, although the same viscosities were used. This is responsible for the steeper spectrum in figure 4. A somewhat smaller viscosity, we believe, would bring the two figures into coincidence.

Table 2 also gives a number of characteristic times for the small scales. Related to these are the times necessary for $\epsilon_i/\langle v^2 \rangle^{\frac{3}{2}}$ and the skewness, both initially zero, to attain their asymptotic values given in table 2. These times are $0 \cdot 45$ s and $0 \cdot 15$ s, respectively. The skewness in table 2 is somewhat less than that found by Orszag & Patterson (1972a, b). Their value is more correct because with our spectrum non-negligible contributions to the longitudinal derivative of the velocity would come from modes beyond our upper cut-off.

When the time integration was begun, E_k began to decrease because the viscosity acts instantaneously while a finite length of time is required for ϵ_i to build up. The energy spectrum begins to rise after $T \sim 1 \cdot 0$ s. No secular changes were observed after $T \sim 2 \cdot 5$ s. The fluctuations in different bands shown in figure 3 are not uncorrelated. Typically, the energy in the second or third shell fluctuates and the rest of the spectrum follows. A tendency towards a step-like pattern is visible in some of the intermediate bands in figure 3. This was also observed by Pouquet & Patterson (1978) and is perhaps due to truncation errors.
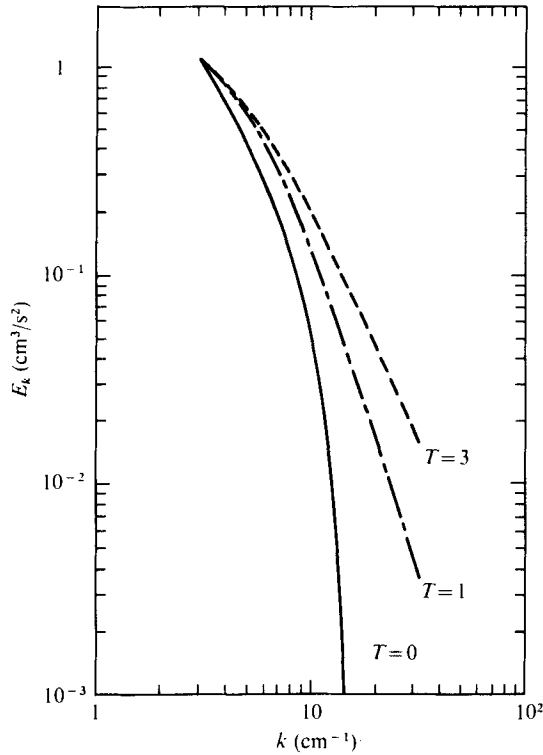
E. D. Siggia and G. S. Patterson

FIGURE 4. Evolution of the initial spectra $E_k = k^{-\frac{5}{3}} \exp[-\frac{1}{10}(k)^4]$ with different initial conditions but the same dissipation parameters as in figure 3. The spectra at $T = 3.0$ and $T = 4.0$ s were identical and gave $R_\lambda \sim 71$. They are somewhat steeper than the spectrum in figure 3 because the random shear is smaller but the dissipation was kept the same.

It was noted above that about 85 % of the energy input was dissipated by the viscosity and the rest by the supplementary damping. This implies both that the second term in (2.2) is not too important (our simulation is only 15 % dishonest) and also that our calculation does not really represent an inertial range despite a good $-\frac{5}{3}$ spectrum. To some extent, however, the viscosity acts like an eddy damping to account for the coupling to modes beyond $k = 32$. The band-averaged viscous dissipation rate normalized by ϵ_i varies from about 0·045 to 0·09 from one end of the spectra to the other, approximately as $k^{\frac{1}{3}}$. For a stationary flow, this will equal the net energy transfer into each shell. There is a tendency, possibly just an artifact of our parameterizations, for energy spectra to appear to be slightly steeper than $-\frac{5}{3}$. Spectra also flatten at small k, probably because of the absence of energy input from modes with $k < 2$. Shell averaging can also distort the energy spectra for small k since

$$\int_{2n}^{2n+2} k^{-\frac{5}{3}} dk$$

does not scale as $n^{-\frac{5}{3}}$ for n small. To compensate for this distortion, the nth shell was plotted at $k = 2n + 1$. The resulting initial spectrum is virtually a straight line with slope 1·67–1·70 on a log–log plot.
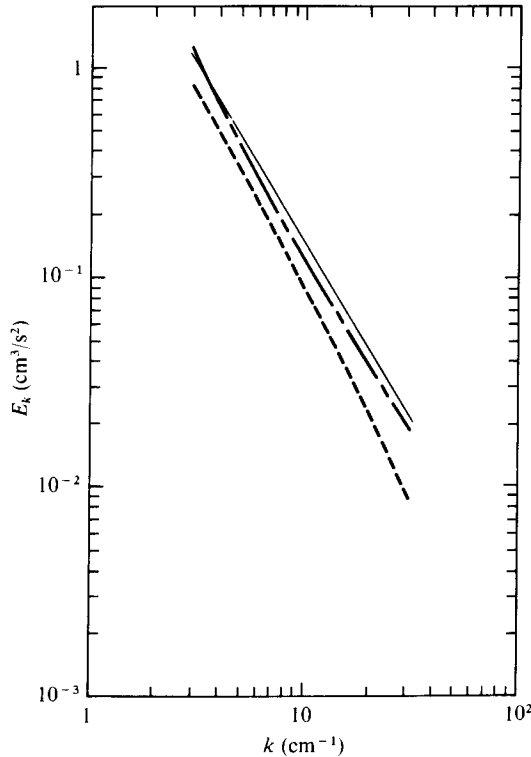
FIGURE 5. Energy spectra generated by the linear forcing defined in (2.3) with $\Omega = 0\cdot4\,\mathrm{s}^{-1}$. The system followed the upper curve until $T \sim 5\cdot5\,\mathrm{s}$, then shifted to the lower curve for $7\cdot0 \lesssim T \leqslant 11\cdot0\,\mathrm{s}$. Additional data are given in table 2. The solid line is a $-\frac{5}{3}$ power law.

The second method employed to keep the energy in our system stationary is a simple linear forcing applied to the first shell:

$$dv_k/dt = \Omega v_k + \ldots, \quad 2 \leqslant k < 4, \tag{2.3}$$

where the dots represent nonlinear terms and the dissipation function in (2.2). This method gives potentially slightly more information from a fixed range of wave-numbers, since the first shell is able to adjust in response to the smaller scales, but it is less physical than the static random shear. Lilly (1972) has used methods of forcing similar to ours in his simulations of two-dimensional flows.

Again the driving mechanism distorts the spectrum slightly. In reality, modes with $k < 2$ should drive both the first shell and successive shells with decreasing efficiency. Equation (2.3) omits energy input to shells beyond the first and leads to excess energy at small k, which is visible in figure 5. The initial behaviour of the energy spectrum was similar to that for the randomly sheared run.

Two sets of data are shown in figure 5 and table 2 for the second run, with (2.3), because the spectrum moved from the upper to lower curves during the interval $5\cdot5\,\mathrm{s} < T < 7\cdot0\,\mathrm{s}$. This behaviour is probably an artifact introduced by (2.3). If some averaged measure of energy transfer is plotted as a function of the energy in the first band, we hypothesize that it can have more than one intersection with the corresponding curve of energy input from (2.3), which is linear with a slope of $2\,\Omega$. The
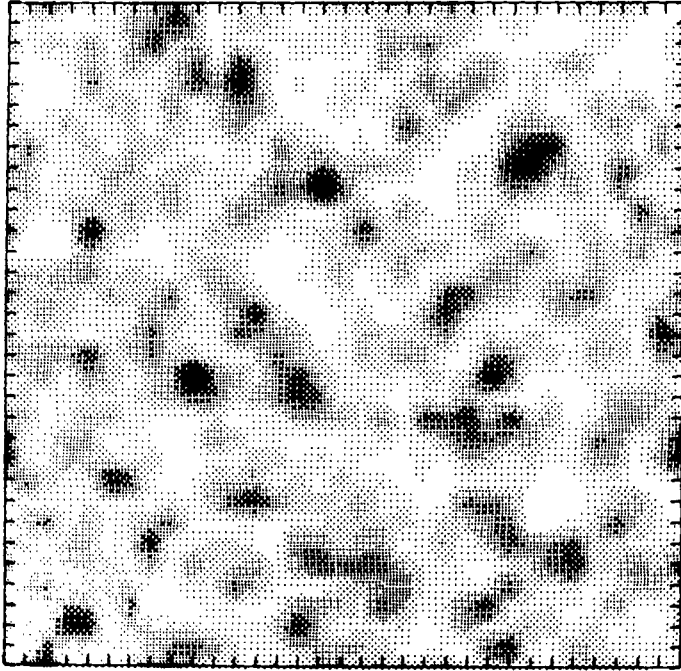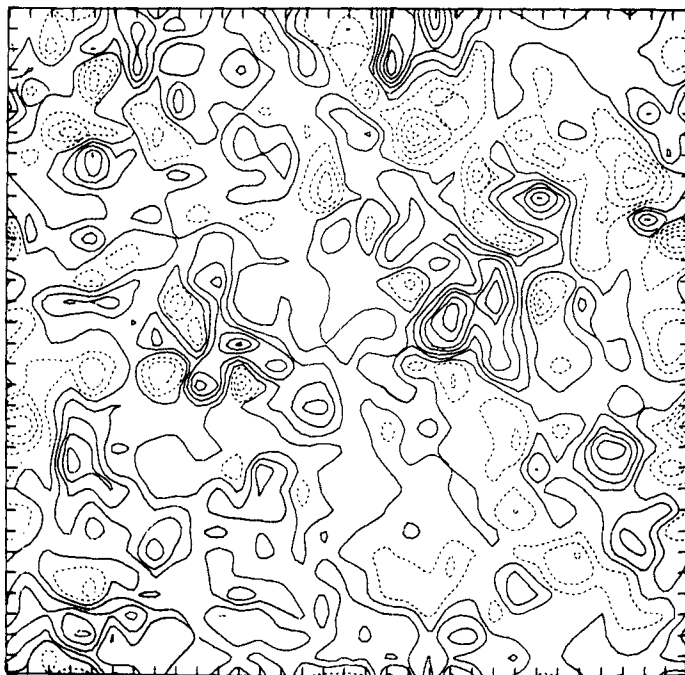
(a)
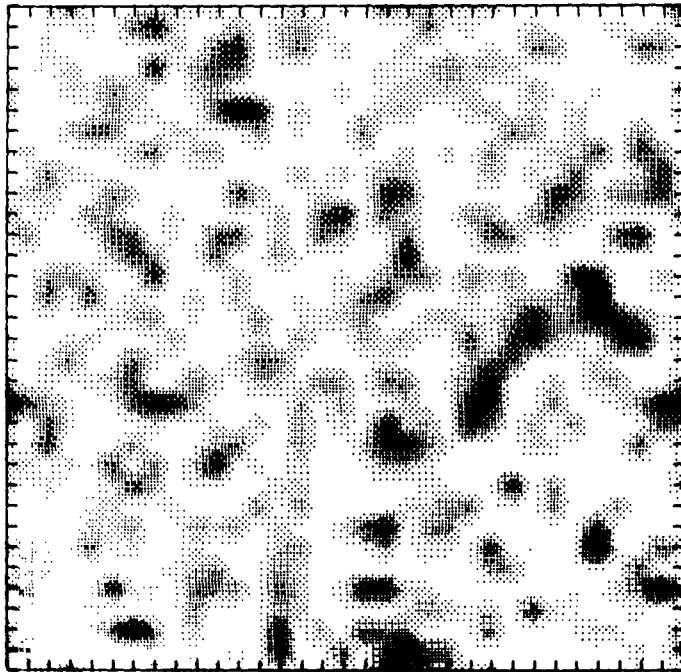
(b)

FIGURES 6 (a, b). For legend see opposite page.

(c)

FIGURE 6. Plots of (a) the mean-square vorticity ω^2, (b) the trace of the rate-of-strain tensor squared when its determinant is positive and zero otherwise, η (det e) tr e^2, and (c) the helicity $\mathbf{v} \cdot \mathbf{\omega}$, all for the same planar slice of data at $T = 0$. The contour interval for the helicity is 10 cm/s². Negative contour lines are dashed. The relation between magnitude and density is linear in the half-tone plots. At $T = 0$, $\langle \det e \rangle = 0$ so a second plot of tr e^2 for det e negative was not drawn. This figure and figures 7 and 8 correspond to the energy spectra for run 1 (cf. figure 3 and the first column of data in table 2).

system can then jump from a nearly stationary state to a possibly stable one. Even so, the spectrum up to $T \sim 5$ s was sufficiently stable that we believe that the corresponding real-space data would be as meaningful as those for the lower branch. The lower curve was somewhat steeper than the upper since the viscosity was not readjusted to maintain the Reynolds number (cf. figure 4).

In the next section, results from the randomly sheared model predominate over those from the linearly forced model because we feel that it is a better approximation to an actual experiment even though it is not strictly homogeneous. The data from either branch in figure 5 are generally within the scatter observed for the first model at different times. This confirms that the particular static shear used for the first run (figure 3) has no appreciable effect on the properties which we shall examine.

3. Numerical results for the 'small' scales

Many authors have noticed that the vorticity plotted from large-scale simulations looks 'spotty', but one can often be misled by ordinary statistical fluctuations. For this reason, the initial data, which are Gaussianly distributed and possess approximately the same energy spectrum as the evolved flows, have been plotted for
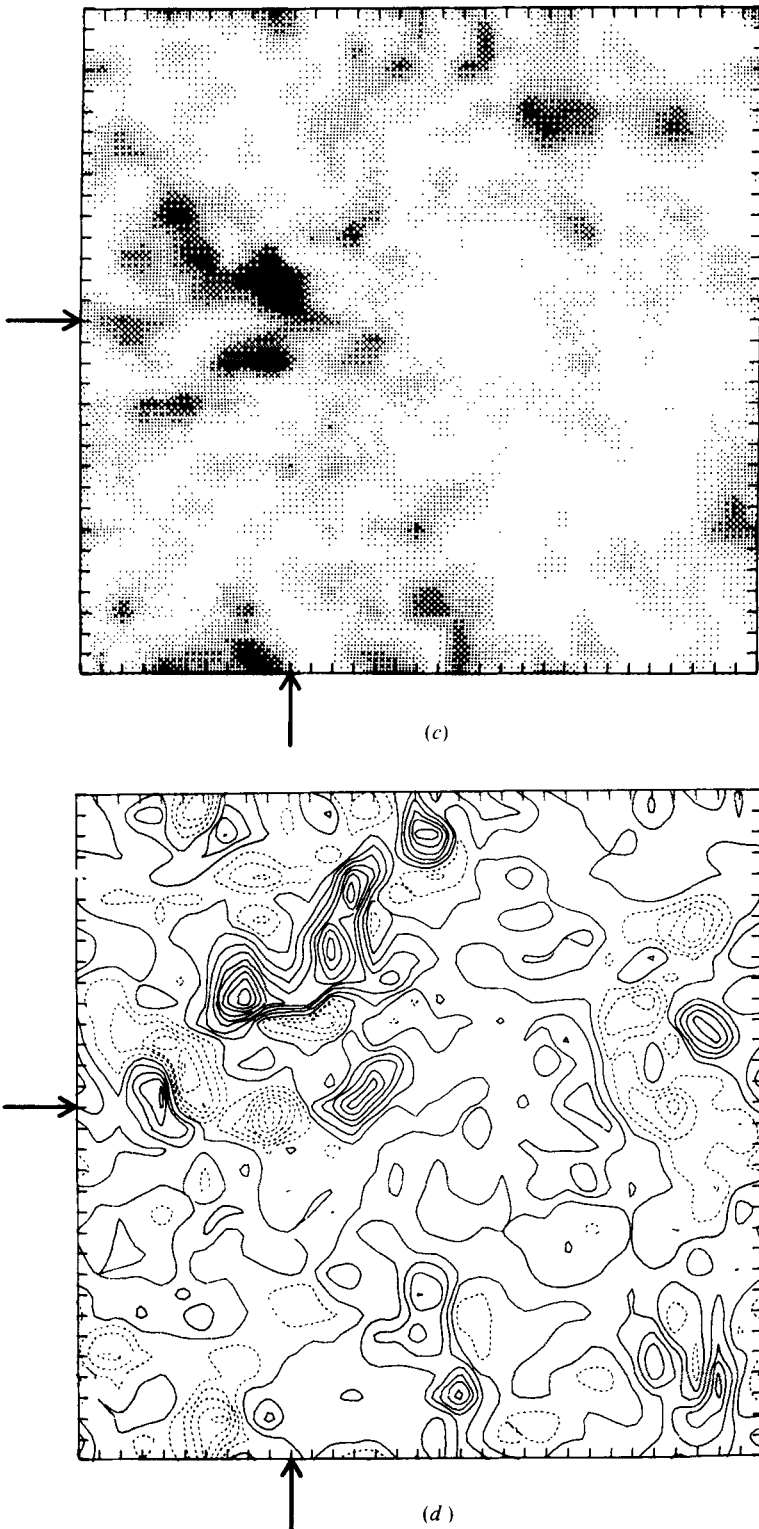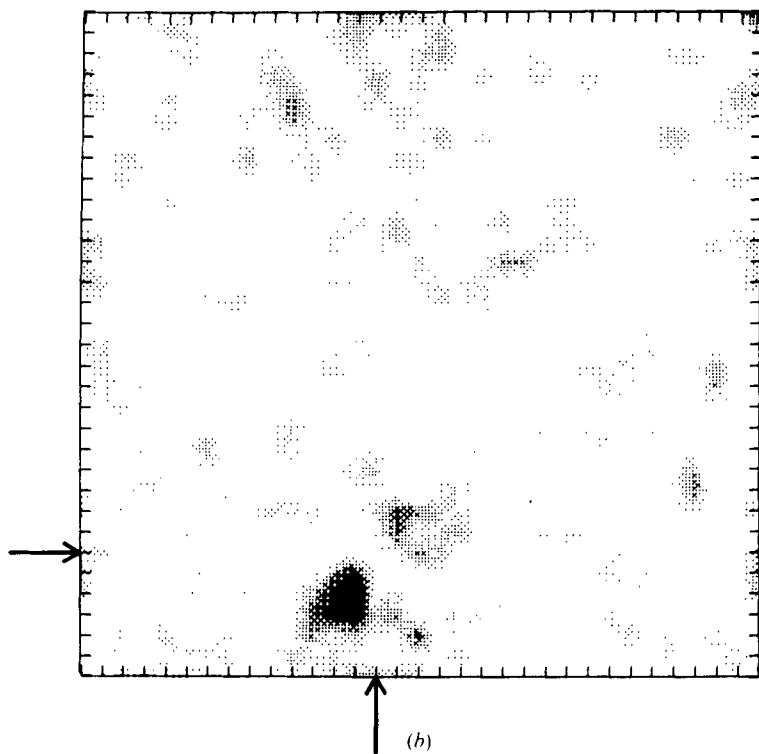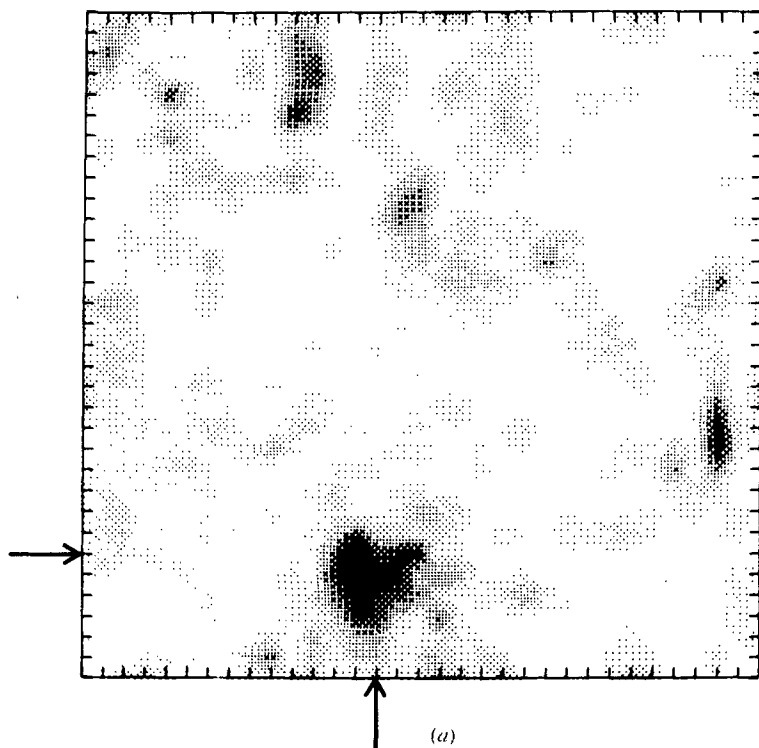
(a)

(b)
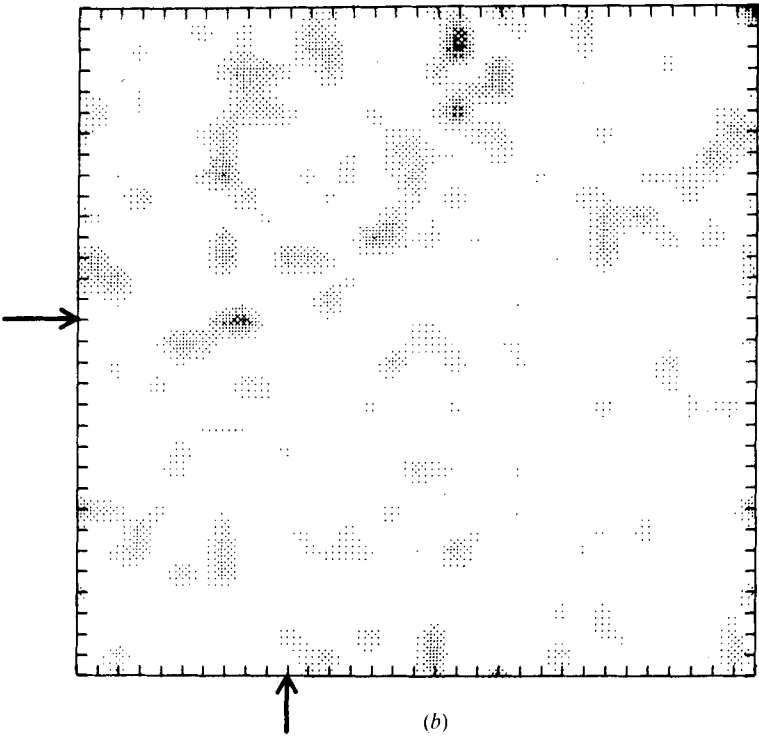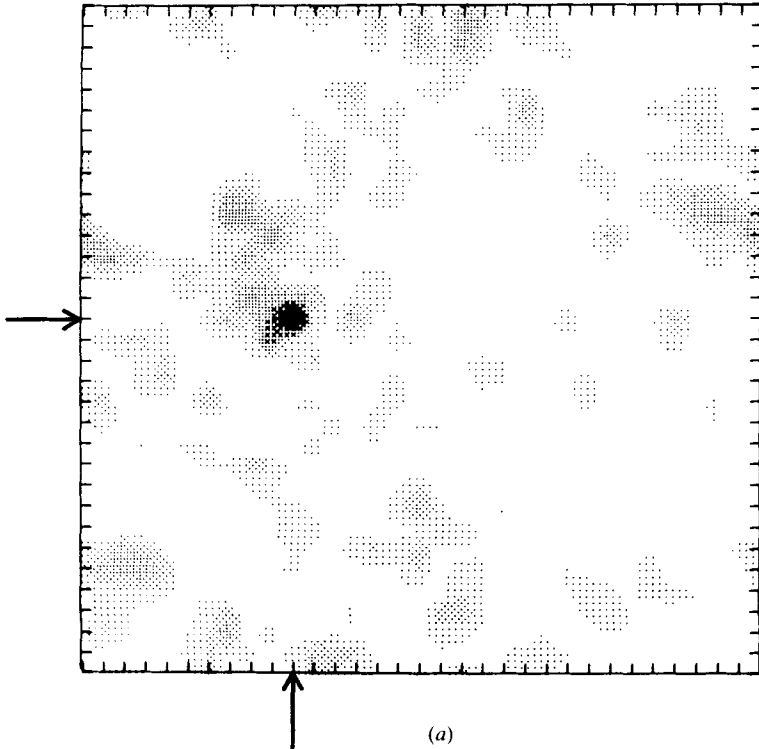
FIGURES 7 (a, b). For legend see opposite page.

(c)

(d)

FIGURE 7. Plots of (a) ω^2, (b) η (det e) tr e^2, (c) $\eta(-\det e)$ tr e^2 and (d) $\mathbf{v} \cdot \boldsymbol{\omega}$ as in figure 6 except that now $T = 6\cdot0$ s and the maxima of ω^2 and tr e^2 have increased by factors of $2\cdot8$ and $1\cdot7$ respectively from their values in figure 6. Corresponding points are marked by arrows.

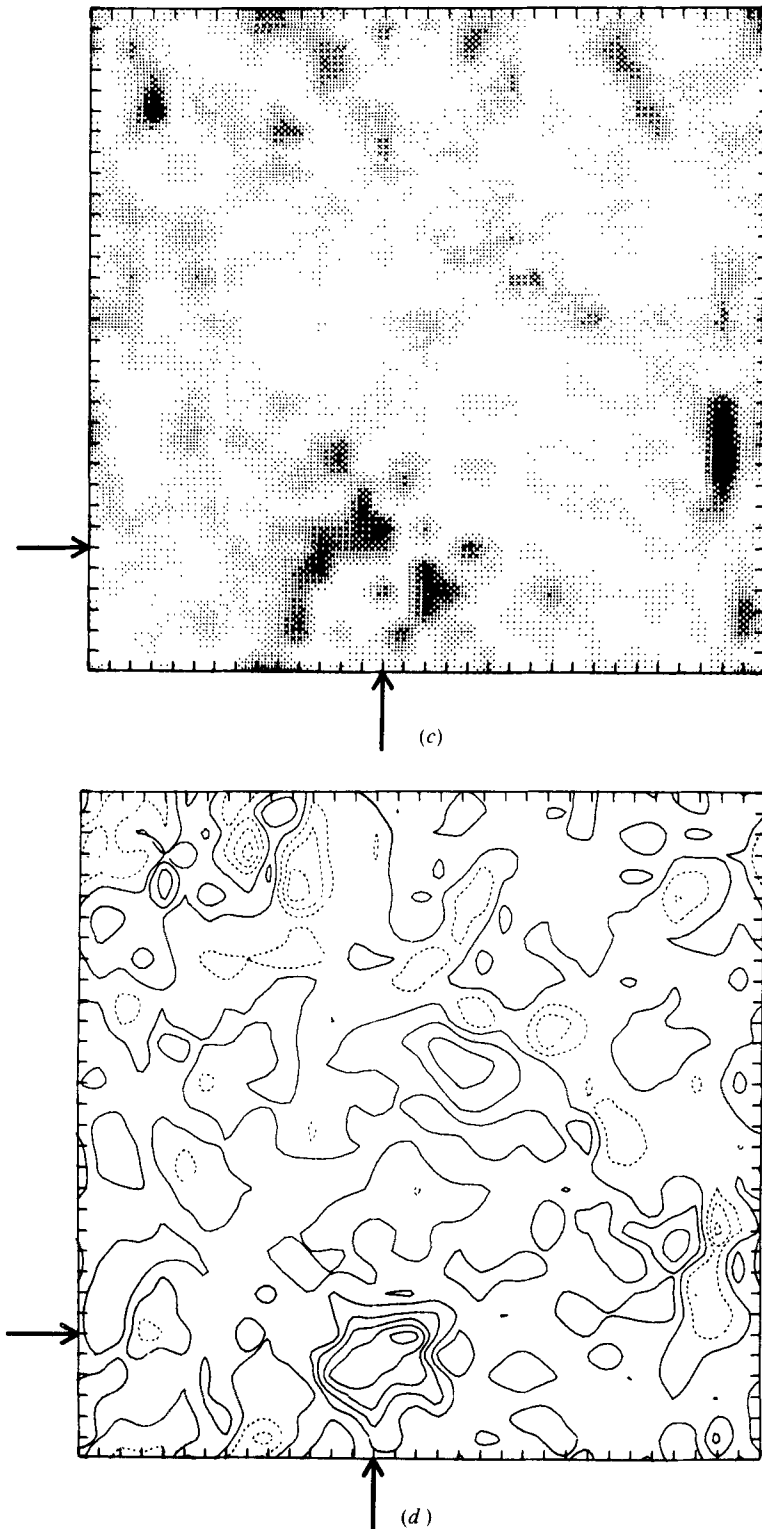(a)

(b)

FIGURES 8 (a, b). For legend see opposite page.

(c)

(d)

FIGURE 8. Same plots as in figure 7 for $T = 7·0$ s. The contour interval in figure 8 (d) is 20 cm/s², and the maxima of ω^2 and tr e^2 are 2·4 and 2·0 times larger than in figure 6. Corresponding points are marked with arrows.
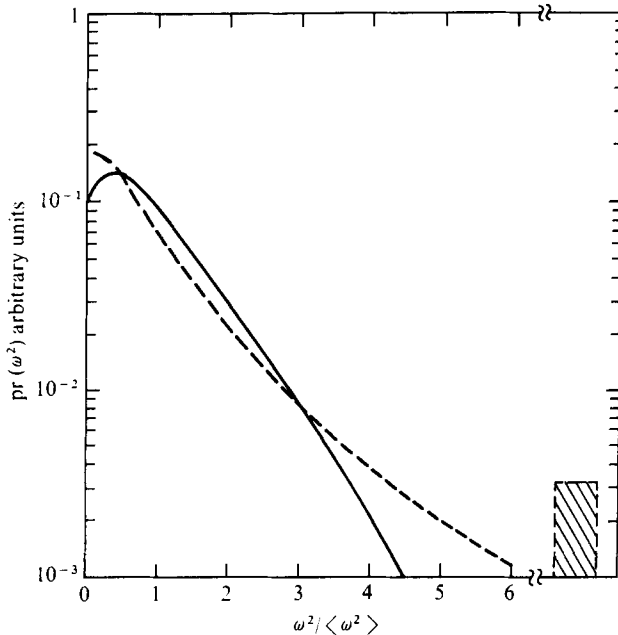
FIGURE 9. Probability distributions of ω^2 in real space at $T = 0$ (solid line) and $T = 4 \cdot 0$ (dashed line) scaled to have the same mean. Actually $\langle \omega^2 \rangle = 245 \, s^{-2}$ at $T = 0$ and $289 \, s^{-2}$ at $T = 4 \cdot 0 \, s$. The shaded rectangle represents data at $T = 4 \cdot 0 \, s$ that exceeded $6 \langle \omega^2 \rangle$. Data at $T = 5 \cdot 0$, $6 \cdot 0$ and $7 \cdot 0 \, s$ were very similar to those shown at $T = 4 \cdot 0$.

comparison. In real space our data occupy a cube of 32^3 points. The density and contour plots were made from planar slices perpendicular to the z axis and periodically extended to a 33×33 mesh. Both plotting routines do some smoothing. Three-dimensional perspective contour plots were also generated but proved a less effective means of displaying the output.

Data at times 0, 6 s and 7 s for ω^2 are shown in figures 6 (a), 7 (a) and 8 (a). The $T = 0$ plot is typical of all the initial slices. Some observers might describe it as 'spotty'. The plot at 7 s is typical of the evolved data while the sample we selected at 6 s was among the most intermittent.

The dramatic difference between the initial and evolved data is partially a consequence of the plotting algorithm, which establishes a linear scale of density spanning the range of values to be portrayed. The maximum data point in figure 7 (a) is $2 \cdot 6$ times larger than the maximum in figure 6 (a), while the minima are both nearly zero. A high value of ω^2 at a few points makes the remaining regions appear less active. If plotted on the same absolute scale, figures 6 (a) and 7 (a) would not look very different, as the smoothed histogram in figure 9 demonstrates. The initial and time-evolved vorticities differ only in the tail of the distribution. The two histograms have been scaled to have the same mean, so the small upward shift of the energy spectrum for $T \gtrsim 3 \, s$, apparent in figure 3, has been factorized out. The average of ω^2 increases by only 20 % so a similar rescaling would not have altered figures 6 (a) and 7 (a).

The rate-of-strain tensor $e_{ij} = \frac{1}{2}(\partial_i v_j + \partial_j v_i)$ controls the local deformation of material surfaces while $\boldsymbol{\omega}$ describes the change in their orientation. The three eigenvalues of e_{ij} are determined by a quantity proportional to the local dissipation rate
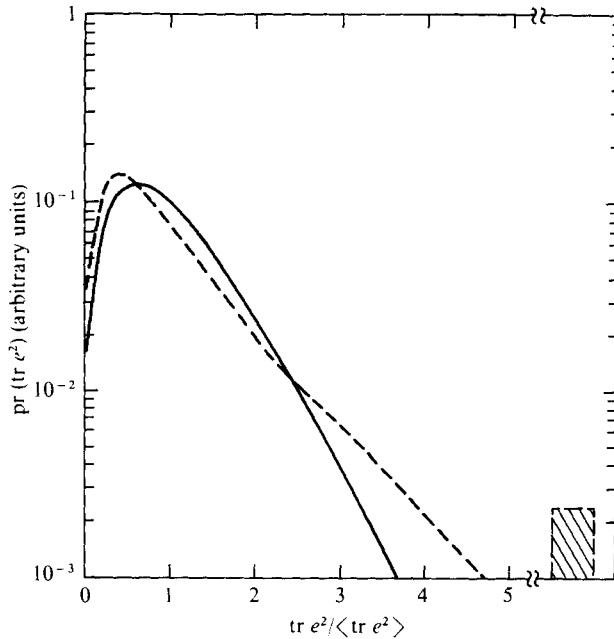
FIGURE 10. Probability distributions of tr e^2 in real space plotted according to the same conventions as in figure 9. At $T = 0$ and $4 \cdot 0$ s, $\langle \mathrm{tr}\, e^2 \rangle = 122$, and $145\,\mathrm{s}^{-1}$ respectively.

tr e^2, the determinant det e of e_{ij} and the incompressibility constraint tr $e = 0$. Depending on whether det e is positive, negative or zero, a spherical surface is deformed into a cigar, pancake or ribbon. Betchov (1956, 1975) has shown for isotropic turbulence that

$$\langle (\partial v_1 / \partial x_1)^3 \rangle \propto \langle \det e \rangle,$$

so we expect regions of negative determinant to predominate. The sign of det e is displayed by plotting tr e^2 twice, once with tr e^2 set to zero at points where det $e < 0$ and then with tr e^2 set to zero whenever det $e > 0$, with the same overall scale in both figures. Contour plots of det e were also made but are not shown, partially because the determinant can be small or zero even when substantial shear exists at the point in question.

The rate-of-strain tensor for one sign of the determinant is shown in figure 6 (*b*) for $T = 0$. There is statistical symmetry between positive and negative values of the determinant. A bias towards a negative determinant is apparent in figures 7 (*b*), 7 (*c*), 8 (*b*) and 8 (*c*). Comparison of the composite plots of tr e^2 again indicates increasing spottiness when $T > 0$. The histogram in figure 10 shows, in analogy with figure 9 for the vorticity, that the initial and evolved flows differ appreciably only in the tails of the distribution.

Figures 8 (*b*) and (*c*) are representative of about 10–20 % of our data that showed a region of intense shear with det $e > 0$. We checked in addition that the determinant was not near zero in most of this region.

A qualitative impression of the correlation between tr e^2 and ω^2 is obtained by examination of the figures. The region of most intense vorticity in figure 7 (*a*) falls between the twin regions of greatest shear in figure 7 (*c*). The region of maximal

	Initial flow	Evolved flow
$\dfrac{\langle \omega^2 \operatorname{tr} e^2 \rangle_c}{\langle \omega^2 \rangle \langle \operatorname{tr} e^2 \rangle}$	0·0	0·22–0·27
$\dfrac{\langle \omega^2 \operatorname{tr} e^2 \rangle_c}{(\langle \omega^4 \rangle_c \langle (\operatorname{tr} e^2)^2 \rangle_c)^{\frac{1}{2}}}$	0·0	0·22–0·26
$\dfrac{\langle \omega^2 |v\omega| \rangle_c}{\langle \omega^2 \rangle \langle |v\omega| \rangle}$	0·33	0·62–0·66
$\dfrac{\langle \omega^2 |v\omega| \rangle_c}{(\langle \omega^4 \rangle_c \langle (v\omega)^2 \rangle_c)^{\frac{1}{2}}}$	0·65	0·53–0·54
$\dfrac{\langle \operatorname{tr} e^2 |v\omega| \rangle_c}{\langle \operatorname{tr} e^2 \rangle \langle |v\omega| \rangle}$	0·0	0·13–0·15
$\dfrac{\langle \operatorname{tr} e^2 |v\omega| \rangle_c}{(\langle (\operatorname{tr} e^2)^2 \rangle_c \langle (v\omega)^2 \rangle_c)^{\frac{1}{2}}}$	0·0	0·15–0·17

TABLE 3. Normalized cross-correlation functions for run 1 (table 2) at $T = 0$ and the spread of values, uncorrelated in time, for $T = 4, 5, 6, 7$ s. Data for the second run are similar. We define $\langle ab \rangle_c = \langle ab \rangle - \langle a \rangle \langle b \rangle$.

vorticity in figure 8(a) is not coincident with the maximum of $\operatorname{tr} e^2$ but correlates better with figure 8(b) than with figure 8(c). A quantitative measure of the cross-correlation is given in table 3. Whether normalized by the average values of the two fields or by the Cauchy–Schwartz bound on $\langle \omega^2 \operatorname{tr} e^2 \rangle_c$, the cross-correlation is not large.

Helicity fluctuations in a turbulent flow are of potential interest for the magnetic dynamo problem (Kraichnan 1976a), but we are unaware of any experimental measurements. For statistically isotropic fields, of course, $\langle |\mathbf{v}.\boldsymbol{\omega}| \rangle = 0$. Our initial data yielded $\langle |\mathbf{v}.\boldsymbol{\omega}| \rangle = 1\cdot14$ cm/s^2, while for later times the average helicity fluctuated between $1\cdot0$ and $2\cdot2$ cm/s^2. Any of these numbers is a factor of 10 larger than what would be expected from the average of 32^3 independent numbers of magnitude $\langle |\mathbf{v}.\boldsymbol{\omega}| \rangle = 11$ or 14 cm/s^2 for the initial and evolved data respectively. The rather large values of $\langle |\mathbf{v}.\boldsymbol{\omega}| \rangle$ which we found are not a statistical fluke, but arise because the velocity is determined by just the largest scales and there exist substantial correlations between the helicity at neighbouring points.

Contour plots of the helicity are shown in figures 6(c), 7(d) and 8(d). The regions of intense helicity appear to be more segregated in the evolved flows though the variation of $\max_r |\mathbf{v}.\boldsymbol{\omega}|$ is not very large and is largely accounted for by the increase in $\langle \omega^2 \rangle$. Histograms of $|\mathbf{v}.\boldsymbol{\omega}|$ show less variation for $T > 0$ than do those for the vorticity or strain rate, probably because helicity is not an inertial-range quantity. Comparison among figures 6, 7 and 8, and the relevant entries in table 3 imply that the helicity is moderately correlated with the vorticity and nearly uncorrelated with $\operatorname{tr} e^2$. The lack of correlation between $|\mathbf{v}.\boldsymbol{\omega}|$ and $\operatorname{tr} e^2$ is to be expected since the latter is conventionally associated with vortex stretching and energy transfer while large values of the helicity indicate that $\mathbf{v} \times \boldsymbol{\omega}$ is small.

The probability distribution of the normalized helicity $|\mathbf{v}.\boldsymbol{\omega}|/|v||\omega|$ appears in figure 11. For the initial flow, it is essentially flat because the velocity and vorticity are determined by opposite ends of the energy spectrum and so in real space are nearly
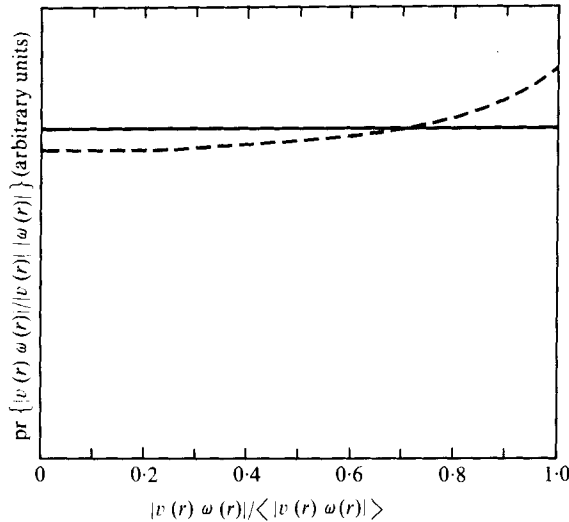
FIGURE 11. Probability distribution of the magnitude of the normalized helicity at $T = 0$ (solid line) and an average of data at $T = 4\cdot0$, $5\cdot0$, $6\cdot0$ and $7\cdot0$ s (dashed line).

independent vectors. This contention is supported by evaluation of

$$\langle v^2\omega^2\rangle/(\langle v^2\rangle\langle\omega^2\rangle) - 1,$$

which is zero initially and varies between $0\cdot01$ and $0\cdot09$ for $T > 3\cdot0$. The probability distribution of the cosine of the angle between two random uncorrelated unit vectors is constant in three dimensions, but would tend to zero at the upper end in higher dimensions. For the evolved data, $\mathbf{v}$ and $\boldsymbol{\omega}$ tend to be parallel. This probably has nothing to do with intermittency. The nonlinear term in the Navier–Stokes equations can be written as the transverse part of $\mathbf{v} \times \boldsymbol{\omega}$ so field configurations with normalized helicity near one may simply evolve more slowly and so be over-represented in the probability distribution.

We explain in the conclusion why it may be of interest to consider the fluctuations in a relative helicity that is Galilean invariant and independent of the energy-containing scales, but no longer conserved. One possible definition is

$$h_V(r) = \left(\mathbf{v}(r) - \frac{1}{V}\int_V \mathbf{v}(r')\,d^3r'\right).\,\boldsymbol{\omega}(r), \qquad (3.1)$$

where V is a symmetrical volume centred about the point r. The relative helicity is a mixture of inertial- and dissipation-range quantities when $\rho = V^{\frac{1}{3}}$ is an inertial-range length. Existing phenomenological theories of intermittency suggest that $\langle h_V^2\rangle$ should scale as $\rho^{\frac{2}{3}-\frac{2}{3}\mu}$ (Mandelbrot 1976; Frisch, Sulem & Nelkin 1978; Nelkin & Bell 1977) or $\rho^{\frac{2}{3}-\frac{5}{9}\mu}$ (Kolmogorov 1962). We shall apply the definition (3.1) to our data by replacing the volume integral by a sum over a cube of lattice points centred at r.

A histogram of $|h_V|$ for 3^3 points is given in figure 12. Data for 2^3 or 4^3 points are similar. The average of $|h_V|$ increases by about 50 % for $T \gtrsim 2$ s while the corresponding change for the true helicity is closer to 25 %. The ratio of the second moments of the two distributions in figure 12 is $4\cdot2$, compared with a ratio of $1\cdot9$ for the actual helicity.
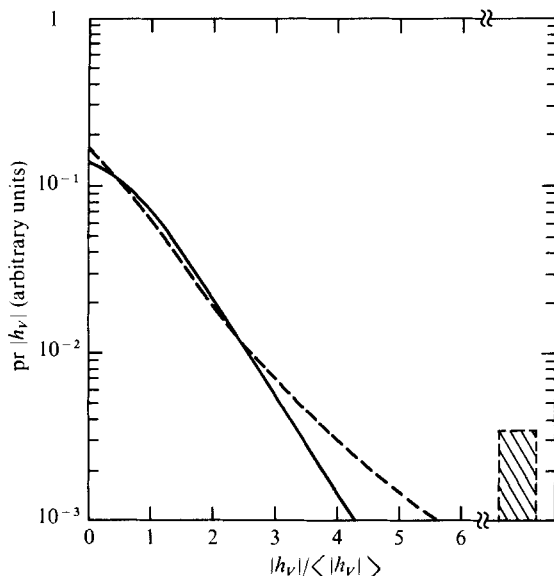
FIGURE 12. Probability distributions with identical first moments for the magnitude of the relative helicity defined in (3.1) for an averaging volume of 3^3 points at $T = 0$ (solid line) and $T = 4 \cdot 0\,\mathrm{s}$ (dashed line). The actual values of $\langle |h_V| \rangle$ are $21 \cdot 0\,\mathrm{cm/s^2}$ and $31 \cdot 1\,\mathrm{cm/s^2}$ at $T = 0$ and $4 \cdot 0\,\mathrm{s}$ respectively.

T	x	y	z
0	3·06	2·99	2·97
4	4·05	3·85	3·80
5	3·89	3·77	3·80
6	3·65	3·84	3·90

TABLE 4. Flatness factors for the longitudinal velocity derivative in the x, y and z directions at times $T = 0$, 4, 5 and 6 s for run 1. Data for the second run in table 2 are similar.

Density plots of kinetic energy would depend largely on the first wavenumber shell and were not drawn. Vector-field plots of two of the three velocity components were made and of course checked against the corresponding vorticity component.

The traditional indicators of intermittency have been the flatness of longitudinal derivatives, high-order longitudinal structure functions and dissipation spectra. They are examined in succession. Computed flatness factors are given in table 4. The initial value of 3·0 is indicative of a Gaussian ensemble and suggests that the aliased flatness computed for $T > 0$ may be physically appropriate (Orszag 1971).

Aliasing arises whenever a spatial average is performed over the product of $n \geqslant 2$ fields defined on a finite mesh in Fourier space. The spatial sum converts into n k-space summations plus the constraint that the sum of the wave vectors equals 0 modulo 32 in our calculation. In an infinite system with no truncation errors, the wave vectors would sum to zero. The aliasing problem is potentially significant for derivative quantities since they weight the largest wave vectors. An aliased skewness was computed from a spatial average of $(\partial v_1/\partial x_1)^3$ and compared with the skewness
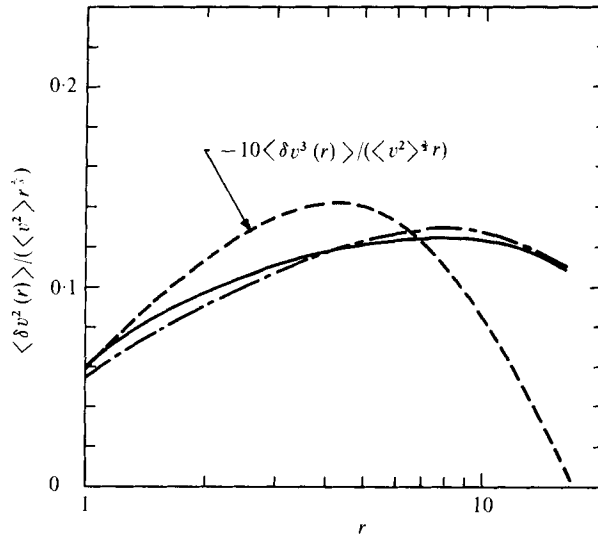
FIGURE 13. Second- and third-order longitudinal structure functions [see (3.3)] normalized by the mean velocity and Kolmogorov's (1941) prediction for their r dependence at $T = 0$ (solid line) and $T = 6.0$ s (dashed lines). The third-order structure function at $T = 0$ was essentially zero and was not reproduced. The distance r is an integer that runs from 1 to 32, although only velocities at points separated by up to half the maximum possible were plotted. The data at $T = 4.0$, 5.0 and 7.0 s looked similar to those shown at $T = 6.0$ s.

factors in table 2, which were computed in Fourier space with the correct constraint. The aliased quantities were 4–9 % too large. Values of the flatness factor for $T > 0$ are definitely larger than 3 but rather less than the experimental values, which are closer to five for our R_λ (see figure 13 of Kuo & Corrsin 1971).

Flatness factors computed for the $T > 0$ data in figure 1 ($R_\lambda \sim 40$) were at least as large as those in table 4. In addition, plots of the vorticity and rate of strain are qualitatively similar to those reproduced. The data in figure 2, on the other hand, gave decidedly smaller flatness factors and the vorticity plots appeared to be more nearly Gaussian. This is to be expected since the modes in the 'tail' at large k are more representative of an equilibrium distribution rather than a turbulent one.

Figure 13 contains plots of the longitudinal second- and third-order structure functions averaged over the three principal directions, e.g.

$$\langle \delta v^m(r) \rangle = \sum_{i=1}^{3} \sum_{\mathbf{R}_n} [v_i(\mathbf{R}_n + \boldsymbol{\pi}_i r) - v_i(\mathbf{R}_n)]^m, \qquad (3.2)$$

where $\mathbf{R}_n$ is a vector with integer components, r an integer, $m = 2$ or 3, and $\boldsymbol{\pi}_i$ a unit vector in the ith direction. The velocity is periodically continued when $R_n^i + r$ exceeds 32.

If the energy spectrum in figure 3 extended over many decades in wavenumber, the second-order structure functions plotted as in figure 13 would be flat. They decrease at small and large separations because a quantity with a separation r is determined by a band of wavenumbers centred at r^{-1}. For large and small r part of this band is absent from the spectrum. The $T = 6$ data probably vary slightly more than their
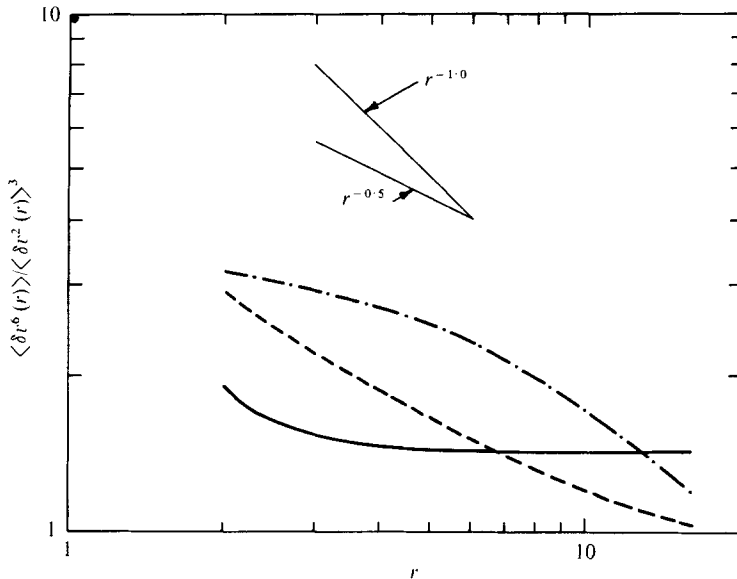
FIGURE 14. Normalized sixth-order structure functions at $T = 0$ (solid line), $T = 4 \cdot 0$ s (upper dashed line) and $T = 6 \cdot 0$ s (lower dashed line). The data at $r = 1$ range from $9 \cdot 0$ to $12 \cdot 0$ for the three curves and are not meaningful for the reasons given in the text. The slopes of $r^{-0 \cdot 5}$ and $r^{-1 \cdot 0}$ cover the range of theoretical and experimental results for the quantity plotted.

counterparts at $T = 0$ because the corresponding energy spectrum is somewhat steeper. The transverse second-order structure functions also do not change appreciably for $T > 0$ and their r dependence is similar to figure 13, though they are somewhat larger.

The third-order structure function is analogous to a discrete skewness and after division by r is commonly used as an order-of-magnitude estimate of the energy transfer down the cascade. Its variation for small r is partially due to the energy dissipation occurring along the cascade. It decreases rapidly to zero near $r = 16$ because the first band of wavenumbers is frozen in a random reflexion-invariant state. Initially, $\langle \delta v^3(r) \rangle$ is an order of magnitude smaller than for $T > 0 \cdot 5$ s and of variable sign. Structure-function measurements have been reported by Van Atta & Chen (1970) and Van Atta & Park (1972).

The high-order structure functions (defined by (3.3) for corresponding m) measured by Van Atta & Park (1972) scaled with separation but departed increasingly from Kolmogorov's (1941) theory with increasing order. We calculated the longitudinal sixth-, ninth- and twelfth-order structure functions but the data became increasingly erratic and only the sixth-order results were reproduced. When scaled by r^2, the sixth-order structure function is either flat or decreasing at small r. This occurs for the same reasons as in figure 13. Judging by the data at $T = 0$ in figure 14, normalizing $\langle \delta v^6(r) \rangle$ by $\langle \delta v^2(r) \rangle^3$ evidently overcorrects for this effect.

The two test slopes in figure 14 correspond to two theoretical predictions. Both begin with Oboukhov's (1962) assumption that the same exponent μ describes the variance of $\delta v^3(r)/r$ and the dissipation fluctuations. This is in accord with the data of Van Atta & Park (1972). If $\langle \delta v^2(r) \rangle$ scaled as $r^{\frac{2}{3}}$, we should obtain a slope of $r^{-0 \cdot 5}$ based on $\mu = 0 \cdot 5$ in figure 14. This is not very different from the lognormal prediction
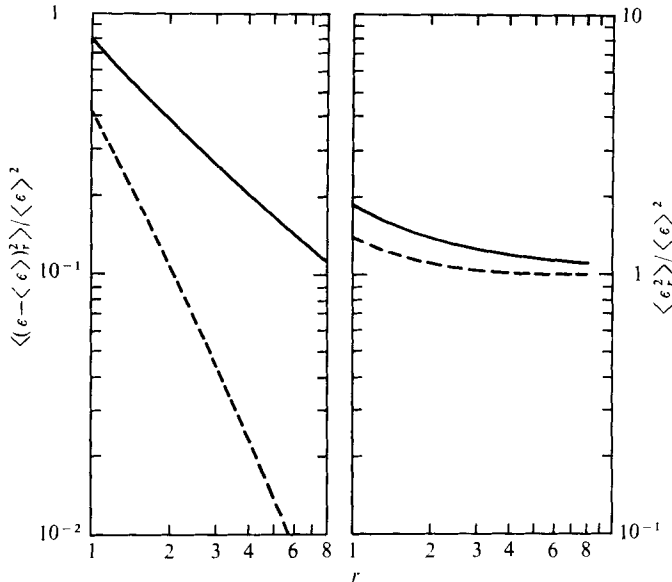
FIGURE 15. Normalized volume-averaged dissipation fluctuations defined in (3.4). Note the different right- and left-hand scales. The initial data are dashed.

$r^{-\frac{1}{3}\mu}$ (Kolmogorov 1962). The steeper line is a consequence of another theory that predicts $\langle \delta v^2(r) \rangle \sim r^{\frac{2}{3}-\frac{1}{3}\mu}$ (Mandelbrot 1976; Frisch *et al.* 1978; Nelkin & Bell 1977). In view of the many possible systematic errors in our calculation, figure 14 is probably consistent with any positive value of μ. The data for $\langle \delta v^{12}(r) \rangle/r^4$ frequently increase with decreasing r but were too noisy to be useful. A time average would have improved the statistics.

Two measures of the fluctuations in the volume-averaged dissipation are plotted in figure 15. We define

$$\epsilon_r = \frac{1}{r^3} \sum_{R_n} \epsilon(R_n), \qquad (3.3)$$

where r is an integer and the sum over R_n runs over a cube of r^3 points centred at some point ρ_n. An average over ρ_n is then performed. The trace of e^2 was used in place of $\epsilon(R_n)$ since all quantities are dimensionless. If $\epsilon(R_n) - \langle\epsilon\rangle$ was uncorrelated at different points, $\langle\epsilon_r^2\rangle - \langle\epsilon\rangle^2$ would scale as r^{-3}, which is nearly the slope of the initial data. The correlations evident in the data at $T = 4$ s need not have any connexion with intermittency. Experiments imply $\langle\epsilon_r^2\rangle \sim r^{-\mu}$ with $\mu \sim 0.5$ (Monin & Yaglom 1975, chap. 25). The increase in $\langle\epsilon_r^2\rangle$ at $T = 0$ for small r is not understood but may indicate aliasing problems.

4. Discussion

It has proved very simple to obtain stationary turbulence that is homogeneous and isotropic to a good approximation. Comparisons between two different methods of driving indicate that none of our results depend sensitively on the particular frozen

shear used in the first run. We also expect that the forcing used in a wave-vector sampling model of intermittency (Siggia 1977),

$$\frac{\partial \mathbf{v}_k}{\partial t} = \frac{\epsilon \mathbf{v}_k}{\sum_{2 \leqslant k < 4} |v_k|^2} + \dots,$$

for $2 \leqslant k < 4$, would have worked equally well here.

We believe that any physically plausible dissipation function with a few adjustable parameters can be tuned to give a reasonable $-\frac{5}{3}$ power-law spectrum. This is in accord with empirical tests of subgrid models, which indicate that refinements of a simple eddy-damping model are seldom worth the increased computational complexity (Clark *et al.* 1977). In the presence of intermittency, however, an eddy damping based on the local shear rate would be superior to the fixed viscosity we used.

Kraichnan (1976a) has demonstrated that helicity fluctuations reduce the magnetic diffusion constant relative to its scalar counterpart even when the net helicity is zero. The precise amount depends on a number of characteristic times which we unfortunately are unable to estimate. It is also conceivable that sufficiently persistent fluctuations in the relative helicity could lead to the growth of randomly oriented but possibly intense fields that move along with their patch of helicity. The possibility of back transfer of magnetic energy or agglutination of small-scale random fields in the absence of injection of net kinetic or magnetic helicity does not seem to have been considered.

Closure models imply that the turbulent cascade is local in Fourier space with most of the energy transferred into a band at k coming from wavenumbers $\gtrsim \frac{1}{10}k$ (Kraichnan 1976b). Our numerical experiments encompassed a wavenumber range of only 16 so imposing a $-\frac{5}{3}$ spectrum by suitable parameterizations might considerably distort the results. These distortions probably could not be uncovered without running a 64^3 simulation.

Comparisons with models of intermittency (Siggia 1977, 1978) are also relevant at this point. These models achieve considerable simplifications by retaining only a fixed subset of the modes in each wavenumber octave. The total number of modes now increases only as the logarithm of the largest wave vector, but the intermittency is temporal. The process for selecting the modes to be retained is equivalent to describing a spatially localized blob of fluid by means of wave packets. The simplest models retain interactions only between adjacent octaves. With these approximations, it is of course much easier to simulate a realistic range of wavenumbers. In addition, the effects of smaller scales on those retained is simple to parameterize in a convincing way. When the model constructed (Siggia 1977) was run with only three octaves, the intermittency was much reduced in comparison with the calculations for four octaves. A simpler model (Siggia 1978) gave no intermittency with three or fewer octaves but effectively an exponent μ of 1 when run with four or more octaves.

An optimistic appraisal of the above models suggests that our simulation should be marginally intermittent, but the numerous possible systematic errors preclude any firm conclusions. We nevertheless believe that it is of interest to compare the various determinants of intermittency both graphically and statistically and to examine the correlations between the vorticity, rate of strain and helicity.

The frequent statement that turbulence simulations look 'spotty' is meaningless unless some randomly distributed velocity field with the same gross characteristics is available for comparison. Our evolved flows did become spottier by generating a few sparse patches of intense vorticity or strain. While this is expected in an intermittent flow, the common statistical measures of intermittency were somewhat ambiguous. It is perhaps appropriate to note here that further analysis of the data used to generate figure 1 showed them to be as intermittent as those for the other runs at a nominally higher R_λ. This of course implies that it is the range of wavenumbers that is limiting the growth of intermittency.

Active regions appeared globular in three-dimensional perspective plots of $\mathrm{tr}\,e^2$ while analogous plots of the mean-square vorticity displayed a number of 'banana' shaped regions.

REFERENCES

BATCHELOR, G. K. 1953 *The Theory of Homogeneous Turbulence*. Cambridge University Press.

BETCHOV, R. 1956 *J. Fluid Mech.* **1**, 497.

BETCHOV, R. 1975 *Phys. Fluids* **18**, 1230.

CLARK, R. A., FERZIGER, J. H. & REYNOLDS, W. S. 1977 Evaluation of subgrid scale turbulence models using a fully simulated turbulent flow. *Stanford Preprint*.

DEARDORFF, J. W. 1970 *J. Fluid Mech.* **41**, 453.

FRISCH, U., SULEM, P. L. & NELKIN, M. 1978 A simple dynamical model of intermittent fully developed turbulence. *J. Fluid Mech.* **87** (to appear).

HERRING, J. R. & KRAICHNAN, R. H. 1972 In *Statistical Models and Turbulence* (ed. M. Rosenblatt & C. Van Atta), p. 148. Springer.

KOLMOGOROV, A. N. 1962 *J. Fluid Mech.* **13**, 82.

KRAICHNAN, R. H. 1976a *J. Fluid Mech.* **75**, 657.

KRAICHNAN, R. H. 1976b *J. Atmos. Sci.* **33**, 1521.

KUO, A. Y.-S. & CORRSIN, S. 1971 *J. Fluid Mech.* **50**, 285.

LILLY, D. K. 1972 *Geophys. Fluid Dyn.* **3**, 289; **4**, 1.

MANDELBROT, B. 1976 *Proc. Journées Mathématiques sur la Turbulence* (ed. R. Teman). Springer.

MONIN, A. S. & YAGLOM, A. M. 1975 *Statistical Fluid Mechanics*, vol. 2. M.I.T. Press.

NELKIN, M. & BELL, T. L. 1977 One exponent scaling for very high Reynolds number turbulence. *Cornell Preprint*.

OBOUKHOV, A. M. 1962 *J. Fluid Mech.* **13**, 77.

ORSZAG, S. A. 1971 *J. Fluid Mech.* **49**, 75.

ORSZAG, S. A. & PATTERSON, G. S. 1972a *Phys. Rev. Lett.* **28**, 76.

ORSZAG, S. A. & PATTERSON, G. S. 1972b In *Statistical Models and Turbulence* (ed. M. Rosenblatt & C. Van Atta), p. 127. Springer.

PATTERSON, G. S. & ORSZAG, A. S. 1971 *Phys. Fluids* **14**, 2538.

POUQUET, A. & PATTERSON, G. S. 1978 *J. Fluid Mech.* **85**, 305.

RILEY, J. J. & PATTERSON, G. S. 1974 *Phys. Fluids* **17**, 292.

SCHUMANN, U. 1975 *J. Comp. Phys.* **18**, 376.

SCHUMANN, U. & PATTERSON, G. S. 1978a Numerical study of pressure and velocity fluctuations in nearly isotropic turbulence. *J. Fluid Mech.* (to appear).

SCHUMANN, U. & PATTERSON, G. S. 1978*b* Numerical study of the return of axisymmetric turbulence to isotropy. *J. Fluid Mech.* (to appear).

SIGGIA, E. D. 1977 *Phys. Rev.* A **15**, 1730.

SIGGIA, E. D. 1978 A model to intermittency in three-dimensional turbulence. *Phys. Rev.* A (to appear).

VAN ATTA, C. W. & CHEN, W. Y. 1970 *J. Fluid Mech.* **44**, 145.

VAN ATTA, C. W. & PARK, J. 1972 *Statistical Models and Turbulence.* (ed. M. Rosenblatt & C. Van Atta), p. 402. Springer.